This is the accepted manuscript made available via CHORUS. The article has been published as:

Magnetization directions and geometries of helical microswimmers for linear velocity-frequency response

Henry C. Fu, Mehdi Jabbarzadeh, and Farshad Meshkati

Phys. Rev. E **91**, 043011 — Published 17 April 2015

DOI: 10.1103/PhysRevE.91.043011

Magnetization directions and geometries of helical microswimmers for linear velocity-frequency response

Henry C. Fu,* Mehdi Jabbarzadeh, and Farshad Meshkati
Department of Mechanical Engineering, University of Nevada, Reno
(Dated: March 26, 2015)

Recently, there has been much progress in creating microswimmers or microrobots capable of controlled propulsion in fluidic environments. These microswimmers have numerous possible applications in biomedicine, microfabrication, and sensing. One type of effective microrobot consists of rigid magnetic helical microswimmers that are propelled when rotated at a range of frequencies by an external rotating magnetic field. Here, we focus on investigating what magnetic dipoles and helical geometries optimally lead to linear velocity-frequency response, which may be desirable for the precise control and positioning of microswimmers. We identify a class of optimal magnetic field moments. We connect our results to the wobbling behavior previously observed and studied in helical microswimmers. In contrast to previous studies, we find that when the full helical geometry is taken into account, wobbling-free motion is not possible for magnetic fields rotating in a plane. Our results compare well quantitatively to previously reported experiments, validating the theoretical analysis method. Finally, in the context of our optimal moments, we identify helical geometries for minimization of wobbling and maximization of swimming velocities.

I. INTRODUCTION

Micro- and nano-robots capable of controlled propulsion have been pursued for a variety of microfabrication and biomedical applications. Biomedical applications include drug delivery[1, 2], tissue manipulation[3–5], and *in vivo* diagnostics and sensing[6–9]. A number of types of microrobots employing different propulsion techniques have been developed, including chemically-powered microrobots dependent on external fuels to create phoretic flows[10–18], externally controlled biotic systems[19], dielectrophoretically manipulated robots[20], and magnetically actuated robots, including those that require a nearby surface[21–24], and those that can swim in bulk fluids[25–35]. In this paper, we focus on magnetically actuated microswimmers in bulk fluids which can be propelled when rotated by an external magnetic field[28–35].

These magnetic swimmers are one of the most promising types of microrobotic systems under current investigation. Compared to other swimmers, magnetic swimmers have advantages for *in vivo* use[36], since they do not require a potentially toxic chemical fuel, and magnetic fields permeate through tissue with little attenuation. Furthermore, swimmers rotated via a magnetic torque produced by field-dipole interactions can be scaled down to micro- and nanoscales unlike those which rely on magnetic forces produced by field gradient-dipole interactions. Although non-helical magnetically rotated swimmers have been reported[35], nearly all such swimmers so far have been helical in geometry[28–30, 32, 34], mimicking the rigid helical flagella of bacteria. Thus, in this paper we focus on the swimming properties of helical geometries.

These swimmers are actuated by a magnetic field of magnitude H, which has a time-dependent direction that rotates with angular velocity $\boldsymbol{\omega}$. In typical experiments, the magnitude of the field is kept constant, while the rotation direction $\hat{\boldsymbol{\omega}}$ and frequency $\omega = |\boldsymbol{\omega}|$ are varied. The direction $\hat{\boldsymbol{\omega}}$ controls the swimming direction (along $\hat{\boldsymbol{\omega}}$), while the frequency ω is most often used to control the speed. Typically, the magnetic field is rotated in a plane perpendicular to its rotation axis, and we will focus on that case here.

One desirable feature for control is a linear relationship between velocity and frequency[37]. This allows simple proportional control of the swimming velocity as frequency is varied, and is especially useful for precise control if the linear relationship extends all the way to zero velocity. One way to achieve a linear velocity-frequency relationship is to maintain a constant axis of rotation as frequency changes[35, 37], but for generic geometries, the axis of rotation varies as frequency is changed while magnetic field strength stays constant[35]. Previous studies have observed these changes in rotation axis for magnetically rotated helices as frequency is varied[37–39]. The change in rotation axis leads to nonlinear velocity-frequency response and hinders ease of control. The rotation axis can be characterized by a "precession angle" (β), which is the angle the axis of rotation makes with the longitudinal helical axis (Fig. 1). For $\beta = 0°$, the swimmer rotates as designed around the helical axis, while for $\beta = 90°$ the swimmer rotates about an axis perpendicular to the helical axis, which has been called "tumbling." Rotation about intermediate axes with $0° < \beta < 90°$ has been called "wobbling." For example, Ghosh *et al.*[39] observed that helices magnetized with moments which were not perpendicular to the helical axis tumble at the lowest frequencies, and show little forward propulsion. As frequency is increased past a critical frequency, the tumbling transitions to wobbling and the precession angle decreases while the velocity increases nonlinearly as frequency is further increased. The precession angle approaches zero and the swimming velocity peaks at the so-

* hfu@unr.edu

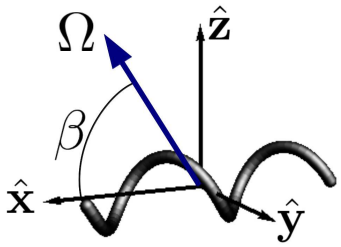

FIG. 1. Rotation of the helix by angular velocity $\mathbf{\Omega}$ can be characterized by the precession angle β.

called step-out frequency. Beyond the step-out frequency, steady rotation is no longer possible since the magnetic torque is not large enough to rotate the swimmer as fast as the field, and the swimming velocity decreases.

The tumbling and wobbling of magnetically rotated helices has been theoretically examined in a number of previous studies. Man and Lauga[40] showed that during wobbling the precession angle scales as inverse frequency using numerics and asymptotics of nearly straight helices. Ghosh *et al.*[39, 41] and Morozov and Leshansky[42] investigated the transition of stability from tumbling to wobbling behavior as frequency increases by treating the rotational dynamics as that of ellipsoids numerically and analytically, respectively.

Two studies have explored what types of magnetization are optimal for helical microswimmers. Recently, Peters *et al.*[37] proposed that wobbling can be eliminated by fabricating superparamagnetic helical microswimmers in a way such that the paramagnetic easy-axis is perpendicular to the helical axis. They showed that microswimmers with such magnetization had much reduced wobbling compared to microswimmers with random easy-axis, as well as improved swimming characteristics. In addition, in a theoretical examination of the rotational and swimming behavior of helices with permanent magnetic dipole, Morozov and Leshansky[42] concluded that for such microswimmers, it is optimal to have the magnetic dipole perpendicular to the helical axis to minimize wobbling.

In previous publications[35, 43], we have described a modeling method for rigid magnetically rotated swimmers that is applicable for arbitrary geometries. The method identifies stable steady rotating orbits of the swimmer for given experimental conditions in terms of the rotation axis of the swimmer and the orientation of the swimmer relative to the magnetic field. Here, we apply our techniques to investigate how the magnetization direction and geometry of helical swimmers can be designed in order to control the rotation axis, reduce wobbling, and produce linear velocity-frequency response, which may enable simplified control, especially at the low speeds required for precise position control.

In the previous work on the rotational dynamics of helical microswimmers mentioned above[39, 41, 42], the rotational dynamics was approximated by the dynamics of an ellipsoid or rod, ignoring chirality and nonaxisymmetry of the helix. Here, we treat the rotational dynamics of a truly helical geometry. We investigate theoretically whether the direction of magnetization can be used to guarantee wobble-free rotation about the helical axis, and find that it cannot. We show that although no moment can completely eliminate wobbling, there are ideal directions of magnetization that are optimal in the sense that they can guarantee linear velocity-frequency relationships. For helices with large aspect ratios (helical length/helical radius), the ideal magnetization directions are close to those suggested previously (i.e., perpendicular to the helical axis) by studies using the ellipsoidal approximation, and we provide a comparison to illustrate how the difference increases as the aspect ratio decreases. We also compare swimming speeds predicted by our theory to those reported for helical swimmers in the literature and find good agreement. Finally, in the context of these ideal directions of magnetization, we investigate what helical geometries minimize wobbling and maximize velocities. Previous work investigating optimal shapes for helical swimmers[44] assumed that the rotation is along the helical axis; here we incorporate the full wobbling dynamics of helices rotated by magnetic fields.

In this work we use both resistive force theory[45] as well as the method of regularized stokeslets[46] to calculate mobility matrices for helical geometries. The resistive force theory is useful for obtaining analytical results which allow exploration of varying helical geometries, while the method of regularized stokeslets allows quantitative comparison with experiments. Resistive force theory is commonly used to investigate both artificial microswimmers as well as biological microswimmers, and by comparing the results of resistive force theory and the method of regularized stokeslets, we also show how thin the helix filament should be for the resistive force theory approximation to hold.

Besides its application to the helical swimmers, the work reported here also provides quantitative validation of the modeling technique used. In [35] and [43] we reported the technique as a method applicable to generic geometries, providing qualitative comparison to observations in [35], but did not quantitatively compare it to experimental results. The agreement between our model and experimental swimming speeds for helices lends support to the use of our model for a wide variety of geometries, including achiral geometries[35]. The potential insights allowed by our technique are demonstrated by investigations of stability in varying magnetic field conditions[43] as well as the rotational dynamics of helices reported here. Our model may be useful for designing effective microswimmers from a much larger geometry space than helical geometries alone. Furthermore, the conclusion that a moment perpendicular to the principal axis of the rotational mobility matrix leads to linear velocity-frequency response applies to nonhelical geometries, which may be useful for general design of microswimmers.

II. MODEL AND METHOD

We follow the general framework for modeling the rotational propulsion of rigid bodies described in Ref. [43]. Here we summarize the essential features for the present study; for more details please see Ref. [43]. In the zero Reynolds number limit appropriate for microswimmers, the instantaneous velocity ($\mathbf{v}$) and angular velocity ($\mathbf{\Omega}$) applied to a rigid body are linearly related to the external force ($\mathbf{F}$) and torque ($\mathbf{N}$) through a 6×6 mobility matrix,

$$\begin{pmatrix} \mathbf{v} \\ \mathbf{\Omega} \end{pmatrix} = \begin{pmatrix} \mathbf{K} & \mathbf{C} \\ \mathbf{C}^{\mathsf{T}} & \mathbf{M} \end{pmatrix} \begin{pmatrix} \mathbf{F} \\ \mathbf{N} \end{pmatrix}. \tag{1}$$

In the above, $\mathbf{K}$, $\mathbf{M}$, and $\mathbf{C}$ are 3×3 submatrices that relate translations to forces, rotations to torques, and translations to torques, respectively. According to this definition $\mathbf{K}$ and $\mathbf{M}$ are positive definite.

In typical experiments, a uniform field interacts with a magnetic dipole to produce zero external force and a net torque $\mathbf{N} = (\mathbf{m} \times \mathbf{H})$, so the instantaneous angular velocity of the swimmer is

$$\mathbf{\Omega} = \mathbf{M}(\mathbf{m} \times \mathbf{H}). \tag{2}$$

A steady solution occurs when the angular velocity of the swimmer is equal to the angular velocity of the rotating magnetic field, so that in a body-fixed frame corotating with the swimmer, the magnetic field and hence angular velocity are constant[47]. Thus a steady solution obeys

$$\mathbf{\Omega} = \boldsymbol{\omega} = \mathbf{M}(\mathbf{m} \times \mathbf{H}), \tag{3}$$

and finding steady solutions amounts to identifying pairs of $\mathbf{H}$ and $\boldsymbol{\omega}$ in the body-fixed frame that satisfy Eq. 3.

In many experiments, the magnetic field is rotated in a plane perpendicular to its rotation axis. In this work, we restrict ourselves to this condition unless explicitly stated otherwise. For such a field, the steady solutions can be found by finding the magnetic field directions which satisfy

$$0 = \hat{\mathbf{H}}^{\mathbf{T}}\mathbf{M}(\mathbf{m} \times \hat{\mathbf{H}}). \tag{4}$$

For example, the direction of the field can be specified using spherical coordinates defined in Fig. 2b,

$$\hat{\mathbf{H}} = (\cos\theta, \sin\theta\cos\phi, \sin\theta\sin\phi)\,, \tag{5}$$

in which case Eq. 4 provides a constraint on the angles (θ, ϕ).

Once the magnetic field direction for a steady solution is identified, the instantaneous swimming velocity can be calculated from Eq. 1 as $\mathbf{v} = \mathbf{CN} = \mathbf{C}(\mathbf{m} \times \mathbf{H})$, which is also constant in the body-fixed frame. The average swimming velocity over a rotation period is the component of the instantaneous swimming velocity along the rotation direction,

$$V_s = \mathbf{v} \cdot \hat{\mathbf{\Omega}}. \tag{6}$$

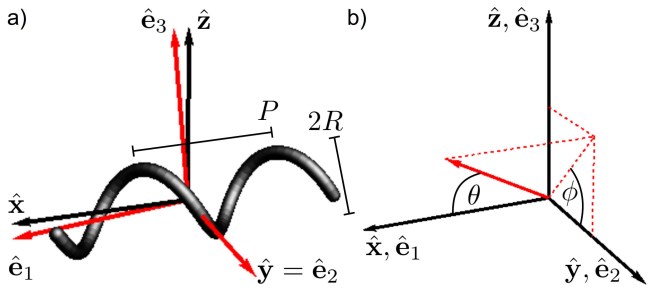

FIG. 2. a) Helix with two turns, pitch P, and radius R. The helical axis is along $\hat{\mathbf{x}}$, and the helix is symmetric about a 180° rotation about $\hat{\mathbf{y}}$. The principal axes of the rotational mobility matrix $\mathbf{M}$ are $\hat{\mathbf{e}}_1$, $\hat{\mathbf{e}}_2$, and $\hat{\mathbf{e}}_3$. b)Angles ϕ and θ used for expressing the magnetic field direction $\hat{\mathbf{H}}$ in spherical coordinates. As specified in text, the angles may be used relative to the symmetry (x, y, z) axes or the principal (1,2,3) axes.

Note that while the instantaneous velocity, which has been used by others as a measure of swimming speed, depends on the origin chosen for the body-fixed frame, the swimming velocity of Eq. 6 is independent of the choice of origin.

One way a linear relationship between swimming velocity and frequency can be achieved if the rotation axis remains constant as the frequency is altered. In that case, Eq. 2 implies that the torque $\mathbf{m} \times \mathbf{H}$ also has constant direction and increases in magnitude linearly with the frequency. Therefore $\mathbf{v}$ also has constant direction and increases linearly with frequency, and so Eq. 6 implies V_s increases linearly with frequency. Thus, maintaining a constant rotation axis for different frequencies can be viewed as a design goal for helical swimmers.

One way to achieve a constant rotation axis is to increase the magnetic field strength proportionally to the frequency as the frequency of the rotation is increased[35]. In this case, it should be clear that the magnetic field direction and rotation direction satisfying Eq. 2 remains fixed while both the field magnitude and frequency increase. However impractically large magnetic fields may be required at higher frequencies so we will search for other ways to achieve linear velocity-frequency response.

Steady solutions can be evaluated for stability by evaluating the eigenvalues of the matrix $\mathbf{Q}$[43],

$$Q_{in} = \left(M_{ij}\epsilon_{jkl}m_k\epsilon_{lmn}H_m - \epsilon_{ijn}M_{jl}\epsilon_{lmo}m_m H_o\right). \tag{7}$$

If the real parts of the eigenvalues are all negative, then the solution is stable, otherwise, it is unstable.

III. MOBILITY MATRIX FOR A HELIX

Consider a helix with centerline specified by

$$\mathbf{r}(\xi) = \xi\hat{\mathbf{x}} + R\cos(2\pi\chi\xi/P)\hat{\mathbf{y}} + R\sin(2\pi\chi\xi/P)\hat{\mathbf{z}}, \tag{8}$$

where P is the helical pitch, R is the helical radius, ξ varies from $-nP/2$ to $nP/2$, and n is the number of turns. (See Fig. 2a.) The parameter $\chi = \pm 1$ controls the chirality of the helix. Note that the arclength $s = \xi/\cos\alpha$, where $\alpha = \arctan(2\pi R/P)$ is the pitch angle.

In these coordinates, the helix is unchanged by the symmetry operation of a 180° rotation about the $\hat{\mathbf{y}}$ axis. Applying the symmetry arguments described in Chapter 5 of Happel of Brenner[48], the mobility matrix takes the form

$$\mathbf{K} = \begin{pmatrix} K_{xx} & 0 & K_{xz} \\ 0 & K_{yy} & 0 \\ K_{xz} & 0 & K_{zz} \end{pmatrix} \tag{9}$$

$$\mathbf{M} = \begin{pmatrix} M_{xx} & 0 & M_{xz} \\ 0 & M_{yy} & 0 \\ M_{xz} & 0 & M_{zz} \end{pmatrix} \tag{10}$$

$$\mathbf{C} = \begin{pmatrix} C_{xx} & 0 & C_{xz} \\ 0 & C_{yy} & 0 \\ C_{zx} & 0 & C_{zz} \end{pmatrix}. \tag{11}$$

In this study, we calculate the mobility matrix for a helix using resistive force theory[45], which is often applied to slender objects such as helical filaments. Although resistive force theory is not always quantitatively accurate[49], it is a convenient way to capture the qualitative dependence of the hydrodynamic mobility matrix on the helical geometry using analytic expressions. Consider a helix moving due to external forces and torques in a quiescent fluid. In resistive force theory, the force per unit length on a segment of the helix is

$$\mathbf{f}(\xi) = [\zeta_{\parallel}\hat{\mathbf{n}}\hat{\mathbf{n}} + \zeta_{\perp}(1 - \hat{\mathbf{n}}\hat{\mathbf{n}})]\mathbf{v}^{rel}(\xi), \tag{12}$$

where $\mathbf{v}^{rel}(\xi)$ is the velocity of the segment relative to the quiescent background, $\hat{\mathbf{n}}(\xi)$ is the tangent to the helix segment, and $\zeta_{\parallel}$ and $\zeta_{\perp}$ are the resistive force theory coefficients. The ratio $\zeta_{\perp}/\zeta_{\parallel}$ depends only logarithmically on the thickness of the helix relative to its pitch, so in this work, we keep the ratio constant ($\zeta_{\perp}/\zeta_{\parallel} = 2$) for our qualitative investigations of the effects of varying helical geometry.

The total force $\mathbf{F}$ and torque $\mathbf{N}$ on the helix are

$$\mathbf{F} = \int_{-nP/2}^{nP/2} \frac{\mathrm{d}\xi}{\cos\alpha}\mathbf{f}(\xi) \tag{13}$$

$$\mathbf{N} = \int_{-nP/2}^{nP/2} \frac{\mathrm{d}\xi}{\cos\alpha}\mathbf{r}(\xi) \times \mathbf{f}(\xi) \tag{14}$$

If the helix undergoes rigid body motions with translational velocity $\mathbf{v}$ and angular velocity $\boldsymbol{\Omega}$, then $\mathbf{v}^{rel}(\xi) = \mathbf{v} + \Omega \times \mathbf{r}(\xi)$. Calculating the total force and torque when $\mathbf{v}$ and $\boldsymbol{\Omega}$ take values along cartesian directions yields the elements of the resistance matrix, which is the inverse of the mobility matrix. In the appendix we list the elements of the resistance matrix. The form of the matrix agrees with that predicted by the symmetry analysis.

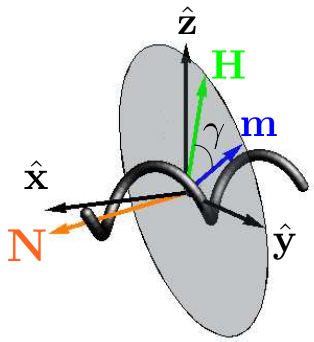

FIG. 3. For a rotation axis along the helical axis ($\hat{\mathbf{x}}$), the torque $\mathbf{N}$ is not in the x-direction, and the moment $\mathbf{m}$ and field $\mathbf{H}$ lie in a plane perpendicular to the torque. As the rotation frequency changes, the angle $\mathbf{H}$ shifts to make a different angle γ with $\mathbf{m}$.

IV. MAGNETIZATION PERPENDICULAR TO THE HELICAL AXIS DOES NOT LEAD TO ROTATION ABOUT THE HELICAL AXIS.

Here we examine whether a permanent magnetic dipole oriented perpendicularly to the helical axis (*i.e.* in the y-z plane), similar to that proposed by Peters *et al.*[37] and Morozov and Leshansky[42], leads to rotation about the helical axis ($\Omega = \Omega\hat{\mathbf{x}}$) and hence no wobbling.

To do so, consider what moments and magnetic fields are needed to yield a rotation axis in the x-direction. The inverse of $\mathbf{M}$ has the same form as $\mathbf{M}$; call its nonzero elements

$$\mathbf{M}^{-1} = \begin{pmatrix} R_{xx} & 0 & R_{zx} \\ 0 & R_{yy} & 0 \\ R_{zx} & 0 & R_{zz} \end{pmatrix}. \tag{15}$$

In order to achieve a rotation $\Omega\hat{\mathbf{x}}$, Eq. 2 requires that the torque $\mathbf{m} \times \mathbf{H} = \Omega(R_{xx}\hat{\mathbf{x}} + R_{zx}\hat{\mathbf{z}})$. Note that the helical geometry leads to off-diagonal elements R_{zx} so that the torque has a z as well as x component. To satisfy this torque, both $\mathbf{m}$ and $\mathbf{H}$ must lie in a plane perpendicular to $\Omega(R_{xx}\hat{\mathbf{x}} + R_{zx}\hat{\mathbf{z}})$ (see Fig. 3). Consider what happens as the frequency of rotation changes. For a given moment $\mathbf{m}$ in that plane, at small frequencies the field $\mathbf{H}$ will point in a direction close to $\mathbf{m}$. As frequency increases, $\mathbf{H}$ will rotate in the plane to make a larger angle with $\mathbf{m}$ and increase the torque. However, since the plane is perpendicular to $\Omega(R_{xx}\hat{\mathbf{x}} + R_{zx}\hat{\mathbf{z}})$ and not $\boldsymbol{\Omega} = \Omega\hat{\mathbf{x}}$, the angle between $\mathbf{H}$ and $\boldsymbol{\Omega}$ must change as the frequency changes. In particular, for almost all frequencies $\mathbf{H}$ will not be perpendicular to $\boldsymbol{\Omega}$. Thus, to achieve a rotation about the helical axis requires a careful tuning of the angle between the field and its rotation axis as the frequency changes, which may be difficult to implement experimentally.

The above argument applies to any moment in the plane perpendicular to the torque. Of those, only one is

also perpendicular to the helical axis, $\mathbf{m} = m\hat{\mathbf{y}}$. Thus for a helical geometry, in contrast to what is suggested by the ellipsoidal approximation, having a moment perpendicular to the helical axis does not lead to rotation about the helical axis for fields perpendicular to rotation. Is there another strategy that could be employed for easier control? Below, we show that although rotation about the helical axis is not easily achievable, one can still choose a moment to obtain linear velocity-frequency response.

V. ROTATION ABOUT THE PRINCIPAL AXIS OF M.

Although the rotational mobility submatrix $\mathbf{M}$ is not diagonal when referred to the symmetry basis $\hat{\mathbf{x}}$, $\hat{\mathbf{y}}$, $\hat{\mathbf{z}}$, it is diagonal when referred to the principal axes $\hat{\mathbf{e}}_1$, $\hat{\mathbf{e}}_2$, $\hat{\mathbf{e}}_3$. Call the respective eigenvalues M_1, M_2, and M_3, which are all positive. For typical helices with large aspect ratio, M_{xz} is small compared to M_{xx} and M_{zz} and one of the eigenvectors of $\mathbf{M}$ will be close to $\hat{\mathbf{x}}$. Let $\hat{\mathbf{e}}_1$ be the principal axis closest to $\hat{\mathbf{x}}$. As the aspect ratio decreases, $\hat{\mathbf{e}}_1$ increasingly deviates from $\hat{\mathbf{x}}$. Below, we show that if the moment is chosen to lie perpendicular to $\hat{\mathbf{e}}_1$, then the rotation axis will be along $\hat{\mathbf{e}}_1$, independent of frequency, and there will be a linear velocity-frequency response.

First, consider how one could obtain rotation along the 1-direction ($\mathbf{\Omega} = \Omega\hat{\mathbf{e}}_1$). Repeating the argument from the previous section but in the principal axis frame, since the mobility matrix is now diagonal the torque is in the 1-direction, and $\mathbf{m}$ and $\mathbf{H}$ lie in the 2-3 plane. In this case, the 2-3 plane is always perpendicular to the rotation axis, so no tuning of the angle between the field and the rotation axis is necessary as frequency is changed.

To be more specific, consider a magnetic moment in the 2-3 plane, $\mathbf{m} = m_2\hat{\mathbf{e}}_2 + m_3\hat{\mathbf{e}}_3$. Specify the field direction using spherical coordinates as in Eq. 5, referred to the principal axes (i.e., θ is the angle between $\mathbf{H}$ and the 1-axis). Then, substituting into Eq. 4, the field directions giving steady solutions satisfy the constraint

$$0 = \sin\theta\cos\theta\left[(M_1-M_2)m_3\cos\phi - (M_1-M_3)m_2\sin\phi\right]. \tag{16}$$

There are two families of solutions to the above constraint equation.

For the first family of solutions, $\theta = \pi/2$ and $\mathbf{H}$ is in the 2-3 plane ($\mathbf{H} = H_2\hat{\mathbf{e}}_2 + H_3\hat{\mathbf{e}}_3$), leading to

$$\mathbf{\Omega} = M_1(m_2H_3 - m_3H_2)\hat{\mathbf{e}_1}. \tag{17}$$

This is the solution discussed two paragraphs above, and is similar to the "propulsive" or "wobbling" solutions found under the ellipsoidal approximation employed by Ghosh *et al.*[39, 41] and Morozov and Leshansky[42, 50]. Since the rotation axis is always in the 1-direction, it will have a linear velocity-frequency response. This solution exists as long as $\omega < M_1mH$, the step-out frequency.

The second family of solutions is specified by

$$\tan\phi = \frac{(M_1 - M_2)m_3}{(M_1 - M_3)m_2} \tag{18}$$

for any value of θ. (Note that this includes solutions to Eq. 16 with $\theta = 0$.) Referred to the principal axes, the corresponding field directions are given by

$$\hat{\mathbf{H}} = \left[\cos\theta, \pm\sin\theta\frac{(M_1 - M_3)m_2}{\sqrt{(M_1 - M_2)^2m_3^2 + (M_1 - M_3)^2m_2^2}}, \pm\sin\theta\frac{(M_1 - M_2)m_3}{\sqrt{(M_1 - M_2)^2m_3^2 + (M_1 - M_3)^2m_2^2}}\right] \tag{19}$$

$$\mathbf{\Omega} = H\left[\mp\frac{M_1m_2m_3(M_2 - M_3)\sin\theta}{\sqrt{(M_1 - M_2)^2m_3^2 - (M_1 - M_3)^2m_2^2}}, M_2m_3\cos\theta, -m_2M_3\cos\theta\right]. \tag{20}$$

V_s can be found by direct substitution of $\hat{\mathbf{H}}$ and $\mathbf{\Omega}$ into Eq. 6, but the expression is not illuminating and too unwieldy to write explicitly here. As we will see using a specific example below, this solution corresponds to "tumbling" rotation.

Note that although any moment in the 2-3 plane has a solution with constant rotation axis along the first principal direction, it may be hard to experimentally realize such moments, since aligning swimmers with the principal, as opposed to symmetry, axes may be difficult. However, $\hat{\mathbf{e}}_2 = \hat{\mathbf{y}}$ is perpendicular to both the symmetry and principal axis, and may be feasible to achieve during fabrication. For example, if helices made by glancing angle deposition[30] are magnetized while still attached to substrate, identification of the 180° symmetry axis corresponds to picking a particular direction parallel to the substrate. Therefore, in some sense magnetization along $\hat{\mathbf{e}}_2 = \hat{\mathbf{y}}$ is the most practical option and we investigate it in more detail below.

A. Moment along 2-direction

For the case of a moment $\mathbf{m} = m_2\hat{\mathbf{e}}_2$ along the 2- (or equivalently y-) direction the above two families of solutions simplify to

$$\mathbf{\Omega} = M_1m_2H_3\hat{\mathbf{e}}_1 = HM_1m_2\sin\phi\hat{\mathbf{e}}_1 \tag{21}$$

$$\mathbf{H} = H(\cos\phi\hat{\mathbf{e}}_2 + \sin\phi\hat{\mathbf{e}}_3) \quad (22)$$
$$V_s = |m_2 H_3| C_{11} = \omega C_{11}/M_1 \quad (23)$$

for the first family and

$$\mathbf{\Omega} = -M_3 m_2 H_1 \hat{\mathbf{e}}_3 = -H M_3 m_2 \cos\theta \hat{\mathbf{e}}_3 \quad (24)$$
$$\mathbf{H} = H(\cos\theta\hat{\mathbf{e}}_1 \pm \sin\theta\hat{\mathbf{e}}_2) \quad (25)$$
$$V_s = |m_2 H_1| C_{33} = \omega C_{33}/M_3 \quad (26)$$

for the second family. It should be clear now that the since the second family rotates about the third principal axis, it is rotating about an axis which is nearly perpendicular to the helical axis and represents the "tumbling" solution. The first family has two solutions with opposite signs of $\mathbf{\Omega}$ for $0 < \omega < |HM_1m_2|$ (corresponding to ϕ and $\phi + \pi$), while the second family has two solutions for $0 < \omega < |HM_3m_2|$ (corresponding to the $\pm$).

Both families are steady solutions, but to determine which solutions are realized experimentally we must evaluate the stability. For the first family, $\mathbf{Q}$ in Eq. 7 is

$$\mathbf{Q} = H \begin{pmatrix} -m_2 M_1 \cos\phi & 0 & 0 \\ 0 & 0 & m_2 M_1 \sin\phi \\ 0 & -m_2(M_1 - M_3)\sin\phi & -m_2 M_3 \cos\phi \end{pmatrix}. \quad (27)$$

The eigenvalues are $\lambda_1 = -M_1 m_2 \cos\phi$ and $\lambda_\pm = (A \pm \sqrt{A^2 + 4BC})/2$, with $A = -m_2 M_3 \cos\phi$, $B = M_1 m_2 \sin\phi$, and $C = -m_2(M_1 - M_3)\sin\phi$. For all helices we have examined, $M_1 > M_3$. Thus $BC = -m_2^2 M_1 (M_1 - M_3)\sin^2\phi < 0$ and the real parts of $\lambda_\pm$ are both negative if and only if $A = -m_2 M_3 \cos\phi < 0$. Therefore stability occurs for $-\pi/2 < \phi < \pi/2$ if $m_2 > 0$ but for $\pi/2 < \phi < 3\pi/2$ if $m_2 < 0$, and in general a stable solution exists for the whole range of ω where there are steady solutions.

For the second family, $\mathbf{Q}$ is

$$\mathbf{Q} = H \begin{pmatrix} \mp m_2 M_1 \sin\theta & m_2(M_1 - M_3)\cos\theta & 0 \\ m_2 M_3 \cos\theta & 0 & 0 \\ 0 & 0 & \mp m_2 M_3 \sin\theta \end{pmatrix} \quad (28)$$

The eigenvalues are $\lambda_3 = \mp m_2 M_3 \sin\theta$, and $\lambda_\pm = (A \pm \sqrt{A^2 + 4BC})/2$, where now $A = \mp m_2 M_1 \sin\theta$, $B = m_2 M_3 \cos\theta$, and $C = m_2(M_1 - M_3)\cos\theta$. In this case, $BC = m_2^2(M_1 - M_3)\cos^2\theta > 0$, so that one of the eigenvalues $\lambda_\pm$ is always positive and the other negative. Thus the second family of solutions is always unstable.

In Fig. 4 we plot the swimming velocity versus the frequency for the first and second families of solutions, for a helix with $n = 2$, $P = 4R$ and chirality $\chi = 1$. In the plots we use the dimensionless frequency specified by $\tilde{\omega} = \omega\zeta_\parallel R^3/(mH)$, and the dimensionless velocity $\tilde{V}_s = V_s\zeta_\parallel R^2/(mH)$. Note that for a given swimmer, the nondimensionalization of V_s that we use is not affected by changes in frequency [unlike another possibility, $V_s/(\omega R)$]; thus, our plots directly reflect the dimensional velocity-frequency plots commonly presented for experimental swimmers. For this chirality $C_{11} > 0$ and $C_{33} < 0$, so the stable first family is the one with positive slope that exists over a larger range.

For this geometry of helix ($n = 2$, $P = 4R$), we can also characterize the rotation via the precession angle β (Fig. 1), which is the angle the axis of rotation makes with the helical axis ($\hat{\mathbf{x}}$). For the first family, this is just the angle between $\hat{\mathbf{e}}_1$ and $\hat{\mathbf{x}}$, giving $\beta = 4.9°$, while for the second family, it is the angle between $\hat{\mathbf{e}}_3$ and $\hat{\mathbf{x}}$, giving $\beta = 85°$.

To conclude this section, we have shown that a moment perpendicular to the principal axis rather than helical axis leads to a linear velocity-frequency response. Although the resulting rotation axis (along $\hat{\mathbf{e}}_1$) is not along the helical axis, for many helices it is relatively close. The dependence of precession angle on helical geometry will be explored in more detail in Section VIII. Finally, note that although we only analytically proved that the propulsion solution is stable and tumbling solution is unstable for moment along the 2-direction, for all helical geometries we have tested, we observed numerically that only the propulsive solution is stable so long as the moment is perpendicular to the first principal axis.

VI. COMPARISON TO EXPERIMENTAL SWIMMING SPEEDS

To validate our results, we compare to experimental results for microswimmers. The examples of microscale swimming magnetic helices in the literature do not exactly correspond with the scenario which we discuss here. Ghosh and Fischer[30] and Ghosh *et al.*[39] examine permanently magnetized helical swimmers with attached heads (which therefore do not have the symmetry of a helix). Other swimmers are soft ferromagnetic helices with heads (e.g., [29]). While Peters *et al.*[37] examine a helical ribbon with no head, their swimmer is paramagnetic. Nonetheless, we can make rough comparisons

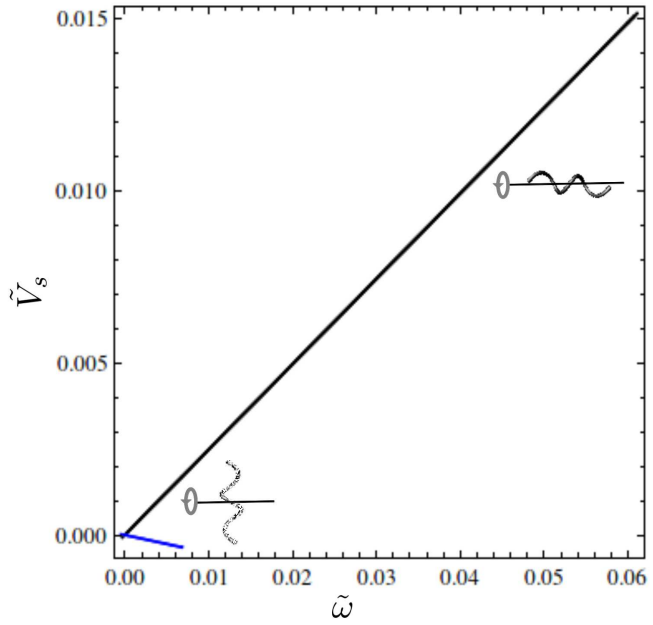

FIG. 4. The swimming velocity vs frequency for the stable solutions of a rotating helix with 2 turns, $P = 4R$, $\chi = 1$, and a moment along the y-direction. The lower branch corresponds to rotation around an axis with precession angle $\beta = 85°$, while the upper branch corresponds to rotation around an axis with precession angle $\beta = 4.9°$

between these and our calculations to ensure that our models are reasonable. Because typically the magnetic moment of these swimmers is not measured the most appropriate measure for comparison is the slope of the velocity-frequency curve when nearly linear behavior is observed. If the frequency is measured in Hertz (revolutions/second), the slope corresponds to the distance traveled per revolution, which is a property dependent only on the geometry of the helix in our model. Therefore, in the following we calculate the slope for the propulsion solution with rotation about the first principal axis of $\mathbf{M}$, and compare to experimental results.

Ghosh *et al.*[39] report artificial swimmers that consist of a spherical head attached to a helix, which has a filament diameter which tapers at the end away from the head. In their paper, they find that swimming speeds are best modeled using an "effective pitch," the amount of translation after one revolution about the helical axis, of 0.08 pitches/revolution. The effective pitch is independent of the moment direction and is a property of geometry of the helix. We model the tail as a helix with constant diameter (see Appendix for details). In Sections V, VII, and VIII, we use resistive force theory to calculate mobility matrices. Although resistive force theory is useful for obtaining analytical expressions that reflect the symmetry of helices and can reveal qualitative trends, it is not expected to be quantitatively accurate for experimental swimmers with thick filaments. We find that resistive force theory is only accurate for filament radii less than $0.035P$, which are much thinner than experimental microswimmers (see Appendix for details). Thus, we calculate the mobility matrix using the method of regularized stokeslets[46] (see Appendix for details). For our model helix, we calculate a velocity-frequency slope of 0.09 pitches, and a precession angle of $< 1°$, which means that the rotation axis is nearly the same as the helical axis. Our calculation does not include the spherical head; its effect can be approximated by calculating the increase in drag in the direction of the helical axis when a head is included in the mobility matrix calculation, and decreasing the effective pitch by the same proportion. With this correction, the estimated velocity-frequency slope is 0.085 pitches/revolution, comparable to the experimental effective pitch of 0.08 pitches/revolution.

Peters *et al.*[37] report superparamagnetic ribbons wound into a helix with no head, which they can rotate nearly without wobble. Again, for such a thick and noncircular cross section resistive force theory is not expected to be accurate so we calculate the mobility matrix using the method of regularized Stokeslets (see Appendix for geometry). The resulting velocity-frequency slope is 2.64 microns/revolution, which is in good agreement with the slopes from Figs. 8 and 9 of Peters *et al.*, which have slopes of $2.6 - 2.8\mu$m/revolution.

In contrast, Ghosh and Fischer[30] report a microswimmer with similar (but smaller) geometry to that of Ghosh *et al.*[39], and find that the velocity corresponds to 0.64 pitches per revolution. However, our model for this helix (see Appendix for details) leads to a velocity-frequency slope about an order of magnitude smaller. We cannot explain the discrepancy; but we note that in addition to being inconsistent with our calculation, the quite large value of 0.64 pitches per revolution is also inconsistent with the effective pitch reported by Ghosh *et al.*[39] as well as biological helical propulsion, which always involves a significant amount of slip of the helix with respect to the fluid.

Based on our numerics and the imprecision of microswimmer geometries, we expect our results to be accurate within 15% (see Appendix for details). Thus, the results for our model are in good overall agreement with the results from two different research groups (Ghosh *et al.*[39] and Peters *et al.*[37]).

VII. COMPARISON TO MOMENT PERPENDICULAR TO HELICAL AXIS

In this section, we calculate the rotational and swimming dynamics for a moment along $\hat{\mathbf{z}}$, which is perpendicular to the helical axis, but not perpendicular to the principal axis. We compare it to the case described in section V to show how moments perpendicular to the helical axis can lead to undesirable swimming properties.

Returning to Eq. 4, but referred to the symmetry axes $\hat{\mathbf{x}}, \hat{\mathbf{y}}, \hat{\mathbf{z}}$, we substitute magnetic field directions specified in spherical coordinates by Eq. 5, where θ is the angle

from the x-direction. This yields

$$0 = -m_3 \cos\phi \sin\theta \left[(M_x - M_y)\cos\theta + M_{xz} \sin\phi \sin\theta \right], \tag{29}$$

which admits solutions for steady orbits in two families.

The first family is specified by

$$\tan\theta = -\frac{M_x - M_y}{M_{xz}\sin\phi} \tag{30}$$

or

$$\mathbf{H} = \frac{[M_{xz}\sin\phi\hat{\mathbf{x}} + (M_y - M_x)\cos\phi\hat{\mathbf{y}} + (M_y - M_x)\sin\phi\hat{\mathbf{z}}]}{\sqrt{M_{xz}^2\sin^2\phi + (M_x - M_y)^2}}. \tag{31}$$

From this equation, $\mathbf{\Omega}$ and V_s can be obtained by substitution into Eqs. 2 and 6, but the expressions are not illuminating so we do not write them here. This solution corresponds to the previously observed wobbling solutions[39].

The second family has $\phi = \pi/2$ and $\mathbf{H}$ in the x-z plane,

$$\mathbf{H} = H(\cos\theta\hat{\mathbf{x}} + \sin\theta\hat{\mathbf{z}}) \tag{32}$$

$$\mathbf{\Omega} = M_y m_z H_x \hat{\mathbf{y}} = H M_y m_z \cos\theta\hat{\mathbf{y}} \tag{33}$$

$$V_s = C_{yy}|m_z H_x| = \omega C_{yy}/M_y, \tag{34}$$

which represents a tumbling solution around the y-axis with linear velocity-frequency response.

Performing a stability analysis on the two families of solutions reveals that the tumbling solutions are stable at the lowest frequencies up to a critical frequency and become unstable at frequencies above the critical frequency ω_c. Below the critical frequency, the first family of solutions is unstable, but above it the first family of solutions is stable. This is similar to the behavior of ellipsoids with magnetic moments which are not perpendicular to the long axis in studies where the geometry of a helix is approximated as an ellipsoid[41, 42].

We can obtain an expression for the critical frequency by examining the stability matrix $\mathbf{Q}$ of Eq. 7 for the second (tumbling) family, which is

$$\mathbf{Q} = H m_z \begin{pmatrix} -M_x\sin\theta & 0 & (M_x - M_y)\cos\theta \\ 0 & -M_y\sin\theta & 0 \\ M_y\cos\theta - M_{xz}\sin\theta & 0 & M_{xz}\cos\theta \end{pmatrix}. \tag{35}$$

The eigenvalues are $\lambda_1 = -M_y \sin\theta$, which is less than zero over the entire range of θ, and $\lambda_\pm = [(A+D) \pm \sqrt{(A+D)^2 - 4(AD-BC)}]/2$. Here, $A = -M_x\sin\theta$, $B = (M_x - M_y)\cos\theta$, $C = M_y\cos\theta - M_{xz}\sin\theta$, and $D = M_{xz}\cos\theta$. In order for the tumbling solution to be stable, both of the $\lambda_\pm$ must also be negative, which requires that both $(A+D) < 0$ and $(AD - BC) > 0$. Using Eq. 33, it can be shown that if $M_x > M_y$ (which holds for helices with aspect ratio larger than 1), then both inequalities are satisfied for

$$\omega^2 < \omega_c^2 = \frac{(m_z M_y H)^2}{1 + (M_x - M_y)^2/M_{xz}^2}. \tag{36}$$

In Fig. 5a, we plot the (nondimensional) velocity vs frequency for the stable solution as a function of frequency, for a helix with $n = 2$, $P = 4R$. The inset shows the transition from the tumbling solution at low frequencies to the wobbling solution above ω_c. Note that both the existence of the transition and the frequency dependence of the wobbling solutions lead to nonlinear dependence of the velocity on frequency, which are disadvantageous for precise swimmer control, especially at low frequencies. At higher frequencies the velocity depends on the frequency nearly linearly. The form of the dependence is similar to that observed for helices by Ghosh *et al.*[39], and modeled for ellipsoids with moment non-perpendicular to the long axis by Ghosh *et al.*[41] and Morozov and Leshansky[42]. However, those previous studies had found that in the ellipsoidal approximation, any moment perpendicular to the helical axis did not have stable tumbling solutions. Here, we show that by taking into account the helical geometry, even moments perpendicular to the helical axis lead to tumbling-wobbling transitions and nonlinear velocity-frequency response. In order to achieve the linear velocity-frequency response, one must instead target rotation about the principal axis using a moment perpendicular to $\hat{\mathbf{e}}_1$.

In Fig. 5b, we plot the precession angle β as a function of frequency for the stable solution. Below the critical frequency, the tumbling solution rotates around the y-axis,

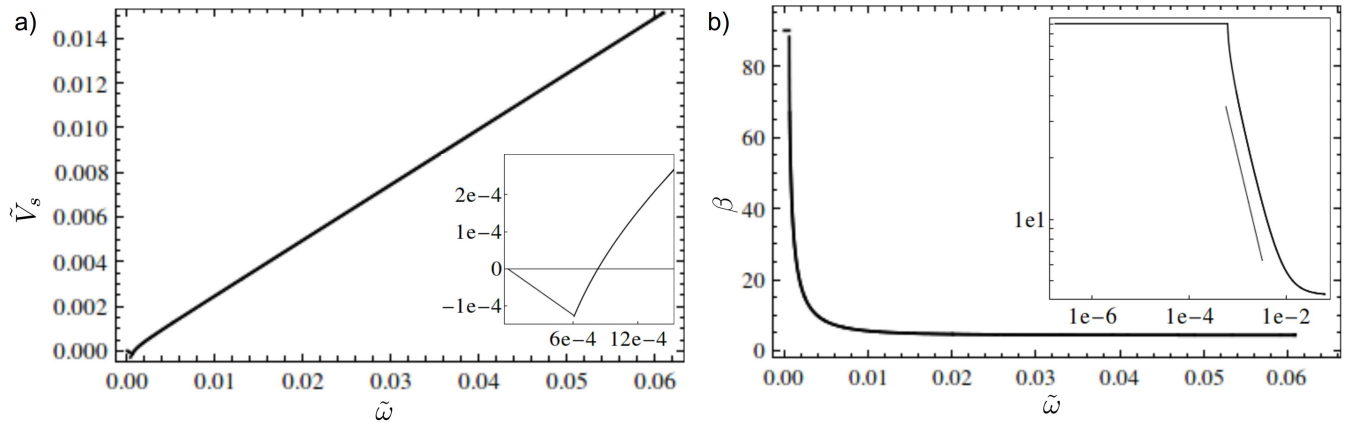

FIG. 5. The a) swimming velocity and b) precession angle vs frequency for the stable solutions of a rotating helix with 2 turns, $P = 4R$, and a moment along the z-direction, which is perpendicular to the helical axis but not the first principal axis. The inset to (a) zooms into the low frequency regime, illustrating the transition between tumbling with rotation about the y-axis at the smallest frequencies, to wobbling rotation with varying precession angle at frequencies above the critical frequency ω_c. The inset to (b) shows a log-log plot of the precession angle vs frequency. The straight line has slope -1, demonstrating the relation $\beta \sim \omega^{-1}$.

so $\beta = 90°$. Above the critical frequency, the wobbling solution starts with $\beta = 90°$ and decreases as frequency increases. Man and Lauga have shown that $\beta \sim \omega^{-1}$ for asymptotically straight helices. In the inset of Fig. 5b, we plot the precession angle as a function of frequency in a log-log plot, to show that for a range of frequencies our precession angle has the same ω^{-1} dependence (straight line).

Fig. 5 shows that for a helix with $n = 2$ and $P = 4R$, the critical frequency is relatively small compared the the step-out frequency, so that the nonlinear response regime is quite small. Is the nonlinear response regime always small? To investigate this, in Fig. 6 we plot the velocity-frequency response for helices with a number of different geometries. The general trend is that as the aspect ratio (helix length/helix diameter) decreases, the critical frequency increases and the nonlinear regime grows in size. For a helix with $n = 1$ and $P = 2R$, ω_c is about a third of the stepout frequency, and the nonlinear regime is a significant portion of the frequency range below stepout. Thus results from the ellipsoidal approximations, which predict that rotation about the helical axis can be achieved for moments perpendicular to the helical axis, fail strongly when the aspect raio of helices is no longer large.

VIII. DEPENDENCE ON HELICAL GEOMETRY

In this section, we continue to investigate the influence of helical geometry on swimming properties. We return to our proposed moment $\mathbf{m} = m_2\hat{\mathbf{y}}$ which is perpendicular to the principal axis $\hat{\mathbf{e}}_1$ and leads to rotation about $\hat{\mathbf{e}}_1$ and a linear velocity-frequency response. For this moment direction, we investigate what helical geometries will lead to a) low precession angles, b) maximum velocity:frequency slopes, and c) greatest maximum velocity.

In Fig. 7 we plot the precession angle of the swimmer as a function of helical pitch for various numbers of turns. Recall that this precession angle is simply the angle between $\hat{\mathbf{e}}_1$ and the x-axis. A small precession angle may be desirable if one wishes to precisely control the location of the tip of the helix during swimming. Typically, the precession angle decreases for larger aspect ratios. Specifically, in order to achieve a precession angle $\beta < 10°$, for $n \geq 2$ the pitch must satisfy $P > 2R$, while for $n = 1$, the pitch must satisfy $P > 8$. These results are in accord with the arguments made by Morozov and Leshansky about the effect of helical geometry on rotational dynamics modeled using ellipsoids[42]; here we quantify how the helical geometry leads to a breakdown of the ellipsoidal approximation.

In Fig. 8 we plot the slope of the velocity-frequency response $\tilde{V}_s/\tilde{\omega}$ of the swimmer as a function of helical pitch for various numbers of turns. Recall that the dimensionless frequency is $\tilde{\omega} = \omega\zeta_\parallel R^3/(mH)$, and the dimensionless velocity is $\tilde{V}_s = V_s\zeta_\parallel R^2/(mH)$; thus the dimensionless slope is nondimensionalized by the helical radius R, *i.e.* $\tilde{V}_s/\tilde{\omega} = (V_s/\omega)/R$. Therefore, Fig. 8 is best interpreted as investigating the variation of the slope as the helical pitch changes but the helical radius stays fixed. For a fixed number of turns, the maximum slope occurs for a pitch around 8-10 R. As the number of turns increases, the slope increases, but saturates around $n = 8$.

In Fig. 9a we plot the maximum velocity $\tilde{V}_s^{max}$ of the swimmer as a function of helical pitch for various numbers of turns. Note that the maximum velocity is distinct from the velocity:frequency slope, since it is the product of the velocity:frequency slope and the step-out

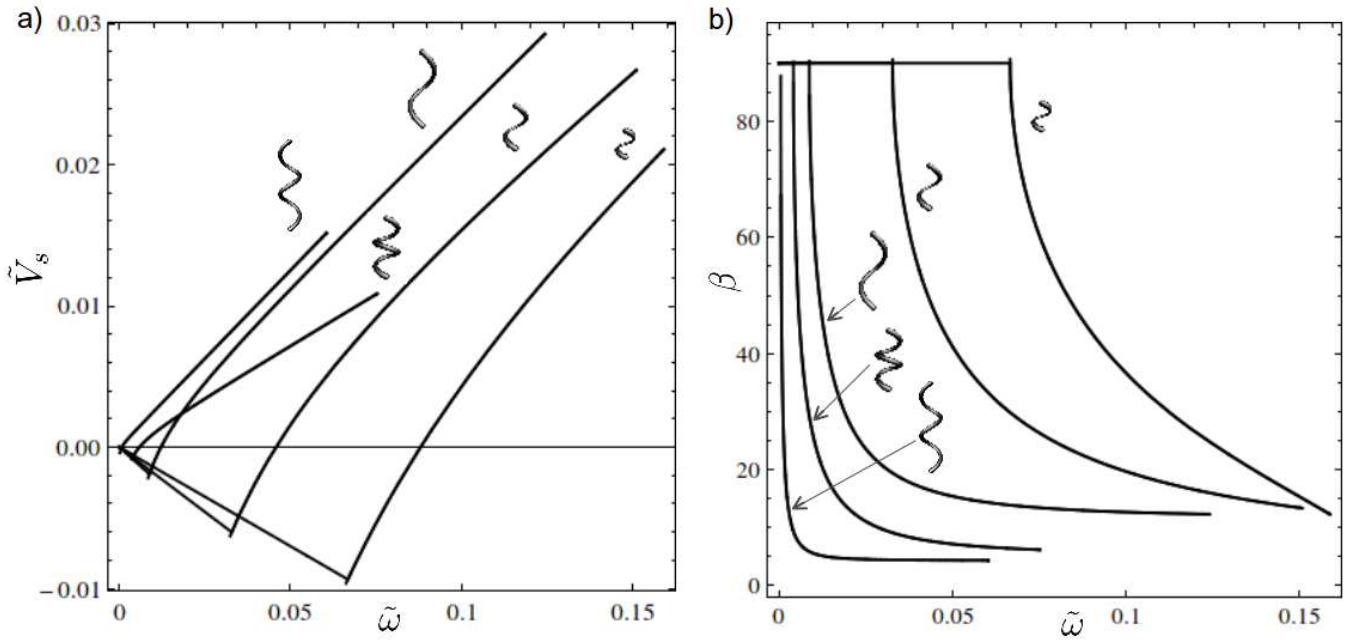

FIG. 6. The swimming velocity (a) and precession angle (b) vs frequency for the stable solutions of rotating helices with moment along the z-direction. From left to right [for (a), as measured by location of sketched helices], and bottom to top [for (b)], curves correspond to helices with: 2 turns, $P = 4R$ [same case as in Fig. 5]; 2 turns, $P = 2R$; 1 turn, $P = 5R$; 1 turn, $P = 3R$; 1 turn, $P = 2R$. Curves are only plotted for frequencies below the step-out frequency. As the aspect ratio (length/diameter) of the helix decreases, a greater portion of frequencies below stepout exhibit tumbling rotation.

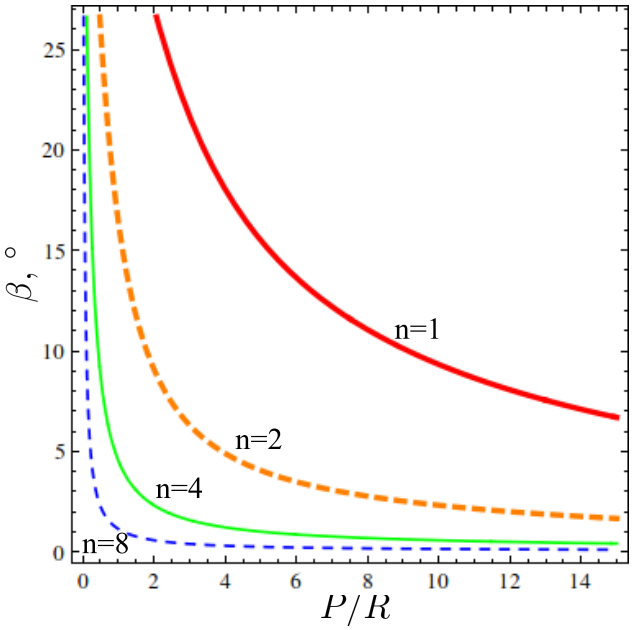

FIG. 7. The precession angle of a helix with moment along the y-direction, perpendicular to the first principal axis, as a function of ratio of helical pitch and radius (P/R), for helices with different numbers of turns: one turn (red, thick solid), 2 turns (orange, thick dashed), 4 turns (green, thin solid), and 8 turns (blue, thin dashed).

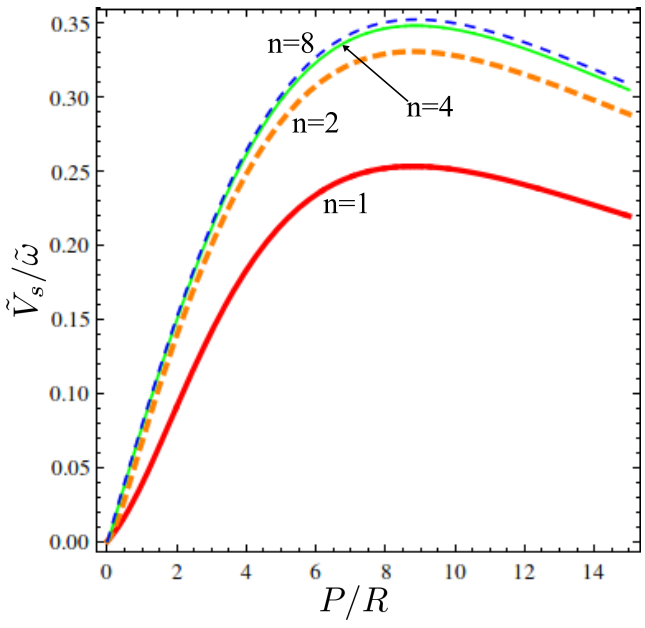

FIG. 8. The velocity:frequency ratio of a helix with moment along the y-direction, perpendicular to the first principal axis, as a function of ratio of helical pitch and radius (P/R), for helices with different numbers of turns: one turn (red, thick solid), 2 turns (orange, thick dashed), 4 turns (green, thin solid), and 8 turns (blue, thin dashed).

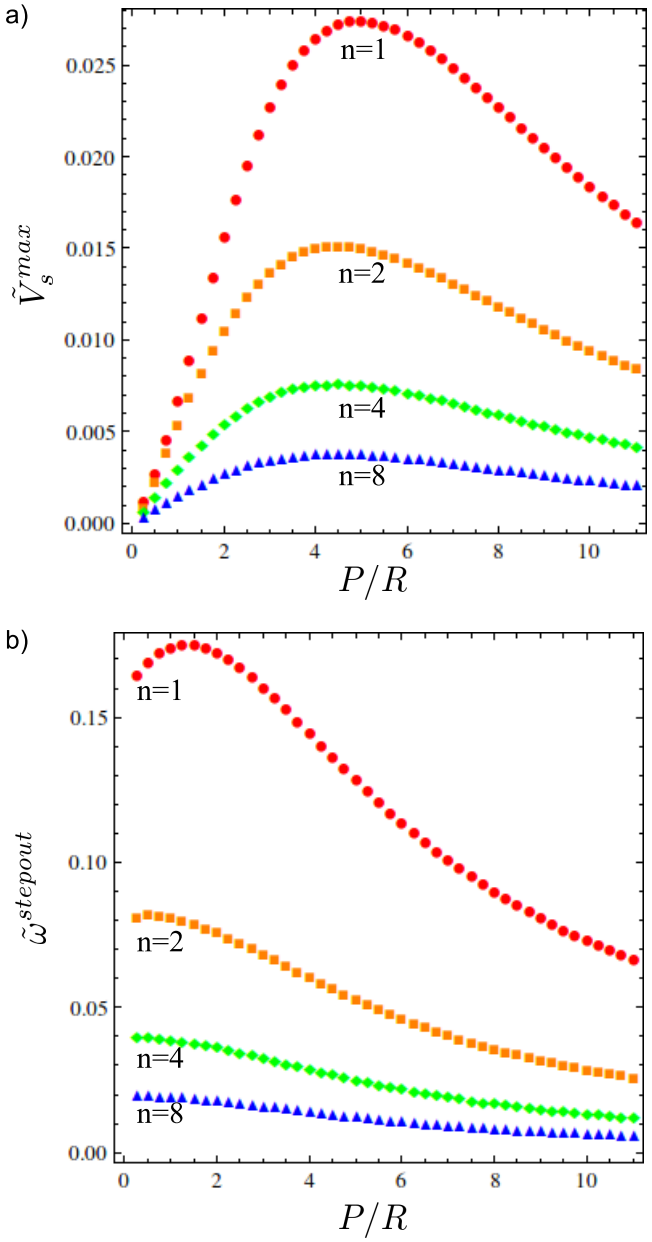

FIG. 9. a) The maximum velocity of a helix with moment along the y-direction, perpendicular to the first principal axis, as a function of ratio of helical pitch and radius (P/R), for helices with different numbers of turns: one turn (red, circles), 2 turns (orange, squares), 4 turns (green, diamonds), and 8 turns (blue, triangles). b) The step-out frequency of the same helices as a function of P/R.

frequency. The choice of whether it is more important to optimize velocity:frequency slope or maximum velocity depends on the application. For a fixed number of turns, the maximum velocity occurs for pitches around 4-6 R, at smaller pitch values than the maximum slope. This can be rationalized by observing how the step-out frequency $\tilde{\omega}^{stepout}$ behaves for different helical geometries, as plotted in Fig. 9b. For a fixed number of turns, the stepout frequency is highest for small pitches near R. Since the maximum velocity is the product of the slope (Fig. 8) and the stepout frequency (Fig. 9b), it at intermediate pitch. Similarly, one can rationalize why swimmers with many turns ($n = 8$) have the largest velocity:frequency slope in Fig. 8 but the smallest maximum velocity in Fig. 9; the large velocity:frequency slope is multiplied by a small step-out frequency (Fig. 9b) to yield small maximum velocities. Based on Fig. 9a, the fastest swimmers would be obtained for $n = 1$ and $P \approx 5R$; however, these would have relatively large precession angles ($\beta \approx 15°$). For $n = 2$ and $P = 4R$, the maximum velocity is about half as much, but the precession angle is reduced to $\beta \approx 5°$.

Note that all the discussion of geometrical dependence in this section uses the helical radius R to nondimensionalize the velocities. Thus, the results should be interpreted as keeping the helical radius R fixed while the pitch and number of turns are varied. For the most common fabrication processes, it is easiest to maintain constant helical radius R as we have done. However, if one wished to design helices with varying R, the results would be different since the scaling of our plotted results with R would need to be taken into account.

IX. DISCUSSION

We investigated the rotational and swimming dynamics of rigid helical microswimmers rotated by an external magnetic field. We investigated how the rotation axis and dependence of velocity on frequency is affected by the direction of magnetic moment and geometry of the helix. We use resistive force theory to obtain mobility matrices that capture the helical geometry of the swimmers, going beyond approximations which treat the rotational dynamics of such swimmers as that of ellipsoids. A linear velocity-frequency response is desirable for control of such microswimmers, and we show that this can be achieved by choosing the magnetic moment to lie perpendicular to the principal axis closest to the helical axis, which results in a single stable branch of solutions which all rotate about the principal axis. We also show that moments which are perpendicular to the helical axis rather than the principal axis lead to nonlinear velocity-frequency response including a transition between low-frequency tumbling and high-frequency wobbling dynamics. Finally, we explored the dependence of swimming properties on helical geometry in the context of our proposed moment perpendicular to the principal axis. Precession angle, the slope of the velocity-frequency response, and maximum velocity were optimized for different helical geometries.

Our work used the resistive force theory to obtain qualitatively accurate mobility matrices for the helical swimmers. The resistive force theory is sufficient to investigate the trends in behavior by providing a convenient way to calculate the mobility matrices for arbitrary helical pitch and radius, and is sufficient to explore quali-

tative features of linear velocity-frequency relationships. While resistive force theory is accurate for very slender helix filaments, we used a boundary element method to obtain quantitatively accurate mobility matrices for the thicker helices fabricated in experiments so far and obtained good agreement between our calculated swimming speeds and experimental results.

We assumed a helical geometry, but if a non-helical geometry is used, the mobility matrix may be more complicated than Eq. 1 due to a loss of the 180° rotation symmetry. For example, although a helical microswimmer with a head or cargo[29, 30] will not have the symmetries we used in our analysis, this can be addressed in two ways. First, if a second head is attached at the other end of the swimmer, the symmetry upon 180° rotation may be restored. Second, even if the swimmer is not symmetric, one can identify the principal axes of its mobility matrix. In that case, the results of Section V apply insofar as a moment perpendicular to a principal axis will admit steady rotational solutions about the principal axis for a range of frequencies. In addition, rotation about the principal axis with the smallest rotational mobility eigenvalue will be stable.

Our work differs from that of Ghosh *et al.*[41] and Morozov and Leshansky[42] in that they approximate the rotational dynamics as those of an magnetized ellipsoid. One conclusion of their work is that a magnetization perpendicular to the helical axis can reduce wobbling and lead to rotation about the helical axis. As shown in Sections IV–VII, using the true helical geometry means that rotation about the helical axis is not actually feasible, and instead rotation about the principal axis, which differs from the helical axis, is a better target. Incorporating the helical geometry, we find tumbling-wobbling transitions and nonlinear velocity-frequency response even when the moment is perpendicular to the helical axis. Although the difference between principal axis and helical axis is small for helices with large aspect ratio, which justifies the ellipsoidal approximation in those cases, the principal axis and helical axis can be significantly different for helices with smaller aspect ratios. Thus, the helical geometry alters the conclusions of those earlier studies in a manner which may be significant for the design of microswimmers. We propose that the most convenient moment to target experimentally is one which is perpendicular to both the first principal axis and the helical axis, rather than any direction perpendicular to the helical axis.

In this work we assumed a permanent magnetic dipole and ignored paramagnetic response of the swimmers. Such response has been addressed by Morozov and Leshansky[50]. In that study, rotational dynamics are approximated as that of an ellipsoid, and we would expect that taking into account the helical geometry may yield similar differences with the ellipsoidal approximation that we have found in the case of a permanent magnetic dipole. Note that in particular the paramagnetic response would be expected to alter the linear velocity-frequency relations found in this work.

In this work we also ignored interactions with boundaries and walls. Although many research groups have explored magnetically rotated microswimmers which "roll" along surfaces, the modeling techniques used here are not directly applicable since the presence of the wall means that the steady solutions found here do not exist; instead there is a time-dependent mobility matrix as the swimmer rotates relative to the wall. Treatment of such cases would require integration of such unsteady rotational orbits, and we do not expect our statements about rotation axes to hold when interaction with surfaces and boundaries becomes strong.

ACKNOWLEDGMENTS

This work was supported by National Science Foundation awards (DMR-1307497 and CMMI-1435652) to HF.

Appendix A: Resistance and mobility matrix for a helix

Here we report the coefficients of the resistance matrix for a helix with pitch P, radius R, and n turns calculated using resistive force theory as described in the main text. Due to the symmetry, the resistance matrix $\mathbf{D}$ has the same nonzero elements as the mobility matrix in the $\hat{\mathbf{x}}$, $\hat{\mathbf{y}}$, $\hat{\mathbf{z}}$ basis,

$$\mathbf{D} = \begin{pmatrix} D_{11} & 0 & D_{13} & D_{14} & 0 & D_{16} \\ 0 & D_{22} & 0 & 0 & D_{25} & 0 \\ D_{13} & 0 & D_{33} & D_{34} & 0 & D_{36} \\ D_{14} & 0 & D_{34} & D_{44} & 0 & D_{46} \\ 0 & D_{25} & 0 & 0 & D_{55} & 0 \\ D_{16} & 0 & D_{36} & D_{46} & 0 & D_{66} \end{pmatrix} \tag{A1}$$

For integer n, the elements above are specified by:

$$D_{11} = (\zeta_{\parallel} R) n \left(\tilde{P} \cos\alpha + 2\pi \tilde{\zeta}_{\perp} \sin\alpha \right) \tag{A2}$$

$$D_{22} = -(\zeta_\parallel R)\pi n \left[(\tilde{\zeta}_\perp - 1)\sin\alpha - 2\tilde{\zeta}_\perp/\sin\alpha\right] \tag{A3}$$
$$D_{33} = D_{22} \tag{A4}$$
$$D_{13} = 0 \tag{A5}$$
$$D_{44} = -(\zeta_\parallel R^3)2\pi n \left[(\tilde{\zeta}_\perp - 1)\sin\alpha - \tilde{\zeta}_\perp/\sin\alpha\right] \tag{A6}$$
$$D_{55} = (\zeta_\parallel R^3)\frac{1}{12}n \left[n^2\tilde{P}^3\tilde{\zeta}_\perp\cos\alpha + 12\pi\tilde{\zeta}_\perp\sin\alpha + \left((15+2n^2\pi^2) - (9-2n^2\pi^2)\tilde{\zeta}_\perp\right)\tilde{P}\cos\alpha\right] \tag{A7}$$
$$D_{66} = (\zeta_\parallel R^3)\frac{1}{12}n \left[n^2\tilde{P}^3\tilde{\zeta}_\perp\cos\alpha + 12\pi\tilde{\zeta}_\perp\sin\alpha + \left((2n^2\pi^2-3) + (9+2n^2\pi^2)\tilde{\zeta}_\perp\right)\tilde{P}\cos\alpha\right] \tag{A8}$$
$$D_{46} = -(\zeta_\parallel R^3)n\tilde{P}\chi \left[(\tilde{\zeta}_\perp - 1)\sin\alpha - \tilde{\zeta}_\perp/\sin\alpha\right] \tag{A9}$$
$$D_{14} = -(\zeta_\parallel R^2)2\pi n\chi(\tilde{\zeta}_\perp - 1)\cos(\alpha) \tag{A10}$$
$$D_{25} = (\zeta_\parallel R^2)\frac{3}{2}n\pi\chi(\tilde{\zeta}_\perp - 1)\cos\alpha \tag{A11}$$
$$D_{36} = (\zeta_\parallel R^2)\frac{1}{2}n\pi\chi(\tilde{\zeta}_\perp - 1)\cos\alpha \tag{A12}$$
$$D_{16} = -(\zeta_\parallel R^2)n\tilde{P}(\tilde{\zeta}_\perp - 1)\cos\alpha \tag{A13}$$
$$D_{34} = 0 \tag{A14}$$

Where $\tilde{P} = P/R$ and $\tilde{\zeta}_\perp = \zeta_\perp/\zeta_\parallel$. The mobility matrix is the inverse of the resistance matrix. Our resistance matrix differs from that reported in Man and Lauga [40] since according to their Eq. 1 their origin is located at one end of the helix, while ours is located along the symmetry axis in the center of the helix. They also include contributions to the moment from local moment densities which resistive force theory ignores.

Appendix B: Quantitative calculation of mobility matrices

In most of the manuscript, we used resistive force theory with the ratio of perpendicular to parallel resistive force coefficients equal to two, which is the expected value in the limit of very slender helical filaments. As the filament radius (a) becomes thicker one can adjust resistive force coefficients; for helices, the following formulas apply[45]:

$$\zeta_\parallel = \frac{2\pi\mu}{\log(0.18P/a)} \tag{B1}$$
$$\zeta_\perp = \frac{4\pi\mu}{\log(0.18P/a) + 1/2}. \tag{B2}$$

However, for the experimental geometries described below (*e.g.* $P = 0.91\,\mu$m, $a = 0.19\,\mu$m), these formulas yield negative $\zeta_\parallel$, implying that they are too thick to be adequately treated by resistive force theory.

To calculate quantitatively accurate mobility matrices, we used the method of regularized stokeslets[46, 51]. Our group has previously implemented the method[52], including to find mobility matrices for the modeling procedure employed in this paper[35, 43], and details of the method can be found in those references.

Here, we provide geometries and results of convergence studies for the helical microswimmers discussed in Section VI. We use these to provide estimates for the error in our calculations of velocity-frequency slopes.

The helical swimmer of Ghosh *et al.*[39] was modeled as a helix with $R = 0.16\mu$m, $P = 0.91\mu$m, 4 turns, and a filament diameter of 0.38μm, as shown in Fig. 10a. This geometry was obtained from Fig 1 of [39]. We performed a convergence study by discretizing the surface with varying number of regularized stokeslets (Fig. 11). The results reported in the main text are for the largest number of elements, 12,134 regularized stokeslets, but we see that even for ≈ 6000 stokeslets there is $< 5\%$ error.

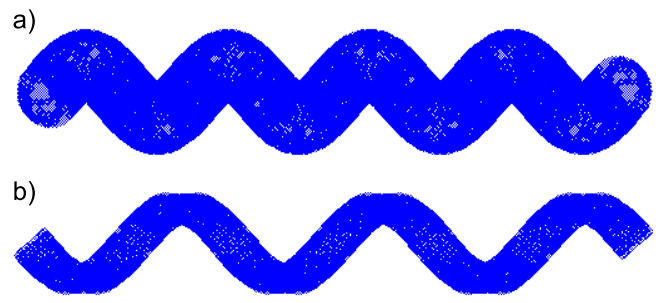

FIG. 10. a) Geometry used to model helix of Ghosh *et al.*[39]. b) Geometry used to model helix of Peters *et al.*[37].

Based on the convergence study above, we can also investigate the accuracy of resistive force theory results for the velocity:frequency slope. In Fig. 12 we compare results from resistive force theory to the method of regularized stokeslets for the geometry above but for varying filament radius. The number of discretization elements for the method of regularized stokeslets varies from 6974 to 15544. For filament radii $a < 0.032\,\mu$m ($a/P < 0.035$), there is less than 5% difference between the resistive force

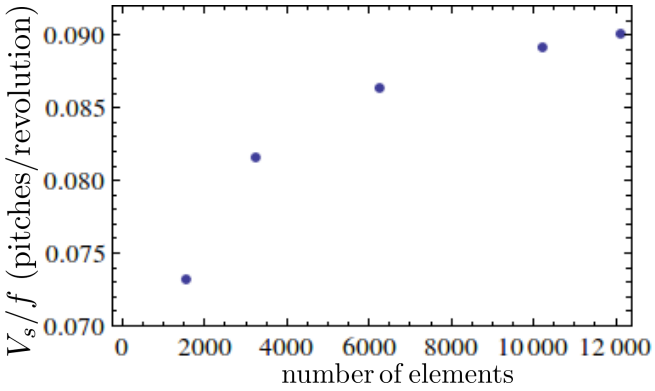

FIG. 11. Convergence study for modeling helix from [39]: velocity-frequency slope as a function of number of regularized stokeslets used in discretization.

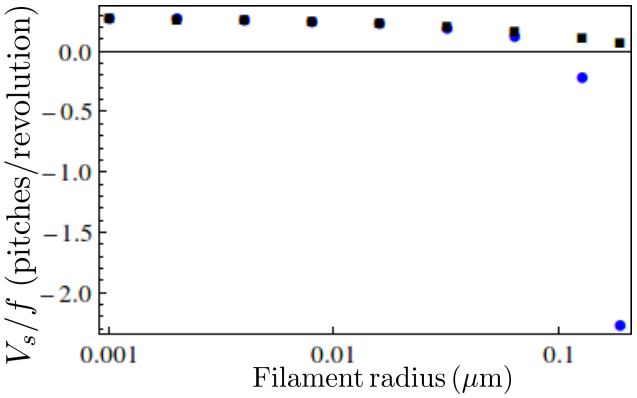

FIG. 12. Comparison of velocity:frequency slopes calculated using resistive force theory (blue circles) and method of regularized stokeslets (blaack squares) as a function of filament thickness. The helix geometry is from [39], but with the filament radius a altered.

theory and method of regularized stokeslets. For resistive force theory, the two largest filament radii plotted ($a = 0.128\,\mu$m and $a = 0.19\,\mu$m) give unphysical negative results, which reflect unphysical resistive force coefficients: Eqs. B1 and B2 give parallel coefficient *larger* than perpendicular coefficient for $a = 0.128\,\mu$m, and *negative* parallel coefficient for $a = 0.19\,\mu$m.

The helical ribbon of Peters *et al.*[37] was modeled as a helix with $R = 2.9\mu$m, $P = 16\mu$m, 3 turns, and a cross section with width 2.8μm and depth 1.5μm. The geometry is shown in Fig. 10b. This geometry was obtained form Fig 3 of [37]. Based on the convergence study performed for the Ghosh *et al.* helix, the reported results are obtained from discretizations involving 5,832 regularized stokeslets, for which we expect discretization error of $\approx 5\%$.

Finally, we note we observed that changes in geometry, particular in the length of the helix, could produce roughly proportional changes in the velocity-frequency slope. Additionally, changing the depth and width of the Peters *et al.* helix to 3.3 μm and 1.8 μm (10-20% changes) reduced the swimming speed by approximately 10%. Based on the imprecision of our measurements of experimental geometries which also do not form perfectly regular helices, we therefore expect an additional 5-10% errors in our results. Combining with the discretization error, we estimate (conservatively) that our calculated velocity-frequency slopes are accurate to within 15%.

[1] G. Dogangil, O. Ergeneman, J. Abbott, S. Pane, H. Hall, S. Muntwyler, and B. Nelson, in *IEEE/RSJ International Conference on Intelligent Robots and Systems, 2008* (2008) pp. 1921–1926.
[2] S. Fusco, G. Chatzipirpiridis, K. M. Sivaraman, O. Ergeneman, B. J. Nelson, and S. Pan, Advanced Healthcare Materials **2**, 1037 (2013).
[3] A. Ferreira, J. Agnus, N. Chaillet, and J. M. Breguet, Mechatronics, IEEE/ASME Transactions on **9**, 508 (2004).
[4] H. Zhang, D. W. Hutmacher, F. Chollet, A. N. Poo, and E. Burdet, Macromolecular Bioscience **5**, 477 (2005).

[5] S. Kim, F. Qiu, S. Kim, A. Ghanbari, C. Moon, L. Zhang, B. J. Nelson, and H. Choi, Advanced Materials **25**, 5863 (2013).

[6] X. Liu, K. Kim, Y. Zhang, and Y. Sun, The International Journal of Robotics Research **28**, 1065 (2009), http://ijr.sagepub.com/content/28/8/1065.full.pdf+html.

[7] S. Martel, J.-B. Mathieu, O. Felfoul, A. Chanu, E. Aboussouan, S. Tamaz, P. Pouponneau, L. Yahia, G. Beaudoin, G. Soulez, and M. Mankiewicz, Applied Physics Letters **90**, 114105 (2007).

[8] M. S. Grady, M. A. Howard, J. A. Molloy, R. C. Ritter, E. G. Quate, and G. T. Gillies, Medical Physics **17**, 405 (1990).

[9] J.-B. Mathieu, G. Beaudoin, and S. Martel, Biomedical Engineering, IEEE Transactions on **53**, 292 (2006).

[10] R. F. Ismagilov, A. Schwartz, N. Bowden, and G. M. Whitesides, Angewandte Chemie **114**, 674 (2002).

[11] W. F. Paxton, K. C. Kistler, C. C. Olmeda, A. Sen, S. K. St. Angelo, Y. Cao, T. E. Mallouk, P. E. Lammert, and V. H. Crespi, Journal of the American Chemical Society **126**, 13424 (2004).

[12] Y. Wang, R. M. Hernandez, D. J. Bartlett, J. M. Bingham, T. R. Kline, A. Sen, and T. E. Mallouk, Langmuir **22**, 10451 (2006).

[13] W. Gao, M. D'Agostino, V. Garcia-Gradilla, J. Orozco, and J. Wang, Small **9**, 467 (2013).

[14] J. Orozco, V. García-Gradilla, M. DAgostino, W. Gao, A. Cortes, and J. Wang, ACS nano **7**, 818 (2012).

[15] K. M. Manesh, M. Cardona, R. Yuan, M. Clark, D. Kagan, S. Balasubramanian, and J. Wang, ACS nano **4**, 1799 (2010).

[16] A. A. Solovev, Y. Mei, E. Bermúdez Ureña, G. Huang, and O. G. Schmidt, Small **5**, 1688 (2009).

[17] J. Gibbs and Y.-P. Zhao, Applied Physics Letters **94**, 163104 (2009).

[18] T. R. Kline, W. F. Paxton, T. E. Mallouk, and A. Sen, Angewandte Chemie **117**, 754 (2005).

[19] E. B. Steager, M. S. Sakar, D. H. Kim, V. Kumar, G. J. Pappas, and M. J. Kim, Journal of Micromechanics and Microengineering **21**, 035001 (2011).

[20] D. L. Fan, F. Q. Zhu, R. C. Cammarata, and C. L. Chien, Nano Today **6**, 339 (2011).

[21] C. E. Sing, L. Schmid, M. F. Schneider, T. Franke, and A. Alexander-Katz, Proceedings of the National Academy of Sciences **107**, 535 (2010).

[22] P. Tierno, O. Güell, F. Sagués, R. Golestanian, and I. Pagonabarraga, Physical Review E **81**, 011402 (2010).

[23] L. Zhang, T. Petit, Y. Lu, B. E. Kratochvil, K. E. Peyer, R. Pei, J. Lou, and B. J. Nelson, ACS nano **4**, 6228 (2010).

[24] W. Xi, A. A. Solovev, A. N. Ananth, D. H. Gracias, S. Sanchez, and O. G. Schmidt, Nanoscale **5**, 1294 (2013).

[25] R. Dreyfus, J. Baudry, M. L. Roper, M. Fermigier, H. A. Stone, and J. Bibette, Nature **437**, 862 (2005).

[26] W. Gao, D. Kagan, O. S. Pak, C. Clawson, S. Campuzano, E. Chuluun-Erdene, E. Shipton, E. E. Fullerton, L. Zhang, E. Lauga, *et al.*, Small **8**, 460 (2012).

[27] O. S. Pak, W. Gao, J. Wang, and E. Lauga, Soft Matter **7**, 8169 (2011).

[28] L. Zhang, E. Ruh, D. Grützmacher, L. Dong, D. J. Bell, B. J. Nelson, and C. Schönenberger, Nano letters **6**, 1311 (2006).

[29] S. Tottori, L. Zhang, F. Qiu, K. K. Krawczyk, A. Franco-Obregón, and B. J. Nelson, Advanced materials **24**, 811 (2012).

[30] A. Ghosh and P. Fischer, Nano letters **9**, 2243 (2009).

[31] U. K. Cheang, D. Roy, J. H. Lee, and M. J. Kim, Applied Physics Letters **97**, 213704 (2010).

[32] F. Z. Temel and S. Yesilyurt, in *Mechatronics (ICM), 2011 IEEE International Conference on* (IEEE, 2011) pp. 342–347.

[33] P. Garstecki, P. Tierno, D. B. Weibel, F. Sagués, and G. M. Whitesides, Journal of Physics: Condensed Matter **21**, 204110 (2009).

[34] L. Zhang, J. J. Abbott, L. Dong, B. E. Kratochvil, D. Bell, and B. J. Nelson, Applied Physics Letters **94**, 064107 (2009).

[35] U. Cheang, F. Meshkati, D. Kim, M. Kim, and H. C. Fu, Phys. Rev. E **90**, 043021 (2014).

[36] J. J. Abbott, K. E. Peyer, M. C. Lagomarsino, L. Zhang, L. Dong, I. K. Kaliakatsos, and B. J. Nelson, The International Journal of Robotics Research **28**, 1434 (2009).

[37] C. Peters, O. Ergeneman, B. J. Nelson, and C. Hierold, in *Micro Electro Mechanical Systems (MEMS), 2013 IEEE 26th International Conference on* (IEEE, 2013) pp. 564–567.

[38] K. E. Peyer, L. Zhang, B. E. Kratochvil, and B. J. Nelson, 2010 IEEE International Conference on Robotics and Automation , 96 (2010).

[39] A. Ghosh, D. Paria, H. J. Singh, P. L. Venugopalan, and A. Ghosh, Physical Review E **86**, 031401 (2012).

[40] Y. Man and E. Lauga, Physics of Fluids (1994-present) **25**, 071904 (2013).

[41] A. Ghosh, P. Mandal, S. Karmakar, and A. Ghosh, Physical Chemistry Chemical Physics **15**, 10817 (2013).

[42] K. I. Morozov and A. M. Leshansky, Nanoscale **6**, 1580 (2014).

[43] F. Meshkati and H. C. Fu, Phys. Rev. E **90**, 063006 (2014).

[44] E. E. Keaveny, S. W. Walker, and M. J. Shelley, Nanoletters **13** (2013).

[45] S. Childress, *Mechanics of swimming and flying* (Cambridge University Press, Cambridge, 1981).

[46] R. Cortez, SIAM Journal on Scientific Computing **23**, 1204 (2001).

[47] Our definition of steady solution excludes the solutions with phase slip discussed by Ghosh *et al.*[41] and Morozov and Leshansky[42].

[48] J. Happel and H. Brenner, *Low Reynolds number hydrodynamics: with special applications to particulate media*, Vol. 1 (Springer, 1983).

[49] B. Rodenborn, C.-H. Chen, H. L. Swinney, B. Liu, and H. P. Zhang, Proceedings of the National Academy of Sciences **110**, E338E347 (2013), http://www.pnas.org/content/110/5/E338.full.pdf+html.

[50] K. I. Morozov and A. M. Leshansky, Nanoscale , Accepted for publication (2014).

[51] R. Cortez, L. Fauci, and A. Medovikov, Physics of Fluids (1994-present) **17**, 031504 (2005).

[52] Y. Hyon, Marcos, T. R. Powers, R. Stocker, and H. C. Fu, Journal of Fluid Mechanics **705**, 58 (2012).